Clinical evaluation of a data-driven respiratory gating algorithm for whole-body positron emission tomography with continuous bed motion

Florian Büther[1], Judson Jones[2], Robert Seifert[1], Lars Stegger[1], Paul Schleyer[2], Michael Schäfers[1,3]

[1]Department of Nuclear Medicine, University Hospital Münster, Münster, Germany

[2]Siemens Healthcare, Knoxville, TN, USA

[3]European Institute for Molecular Imaging, University of Münster, Münster, Germany

Corresponding author: Dr. rer. medic. Florian Büther

Department of Nuclear Medicine, University Hospital Münster

Albert-Schweitzer-Campus 1

48149 Münster, Germany

E-Mail: butherf@uni-muenster.de

Tel.: +49 251 8349336

Fax: +49 251 8347363

Word count: 4998

Running title: Data-driven gating for CBM-PET/CT

ABSTRACT

Respiratory gating is the standard to overcome respiration effects degrading image quality in positron emission tomography (PET). Data-driven gating (DDG) using signals derived from PET raw data are promising alternatives to gating approaches requiring additional hardware. However, continuous bed motion (CBM) scans require dedicated DDG approaches for axially-extended PET, compared to DDG for conventional step-and-shoot scans. In this study, a CBM-capable DDG algorithm was investigated in a clinical cohort, comparing it to hardware-based gating using gated and fully motion-corrected reconstructions.

Methods: 56 patients with suspected malignancies in thorax or abdomen underwent whole-body ^{18}F-FDG CBM-PET/CT imaging using DDG and hardware-based respiratory gating (pressure-sensitive belt gating, BG). Correlation analyses were performed on both gating signals. Besides static reconstructions, BG and DDG were used for optimally-gated PET (BG-OG, DDG-OG) and fully motion-corrected PET (elastic motion correction; BG-EMOCO, DDG-EMOCO). Metabolic volumes, SUV_{max} and SUV_{mean} of lesions were compared amongst the reconstructions. Additionally, the quality of lesion delineation in different PET reconstructions was independently evaluated by three experts.

Results: Global correlation coefficients between BG and DDG signals amounted to 0.48±0.11, peaking at 0.89±0.07 when scanning the kidney and liver region. In total, 196 lesions were analyzed. SUV measurements were significantly higher in BG-OG, DDG-OG, BG-EMOCO and DDG-EMOCO compared to static images ($P<0.001$; median SUV_{max}: static, 14.3±13.4; BG-EMOCO, 19.8±15.7; DDG-EMOCO, 20.5±15.6; BG-OG, 19.6±17.1; DDG-OG, 18.9±16.6). No significant differences between BG-OG and DDG-OG, and BG-EMOCO and DDG-EMOCO, respectively, were found. Visual lesion delineation was significantly better in BG-EMOCO and

DDG-EMOCO than in static reconstructions (*P*<0.001); no significant difference was found comparing BG and DDG (EMOCO, OG, respectively).

Conclusion: DDG-based motion-compensation of CBM-PET acquisitions outperforms static reconstructions, delivering qualities comparable to hardware-based approaches. The new algorithm may be a valuable alternative for CBM-PET systems.

Key words: PET, PET/CT, respiratory motion, gating, motion correction

INTRODUCTION

Respiratory motion is a source of image degradation in positron emission tomography (PET) and combined PET/computer tomography (CT) of the thorax and the abdomen (*1*). It leads to effective resolution losses, image blurring, apparent decreased tracer uptake and increased volumes of lesions, and potentially lower detection rates for malignancies (*2*).

Hardware-based gating approaches, using additional equipment to record the respiration of the patient, are widely considered as the reference standard to minimize these effects (*3-5*). The two most frequently utilized systems use sensors measuring pressure changes within a belt around the belly (*6*), and camera systems monitoring the motion of markers placed on the patient (*7*).

In contrast, data-driven gating (DDG) approaches derive respiratory waveforms from PET raw data (*8*). Different DDG methods have been investigated in the past (*9-13*), and first clinical evaluations have proven their efficacy (*14-17*). All these studies were performed with limited amounts of bed positions in conventional "step-and-shoot" mode where temporal fluctuations of respiratory frequencies within measured data can be assumed to reflect respiratory motion. However, for well-established "continuous bed motion" (CBM) scans (*18*), this no longer holds true, as the moving bed introduces additional time dependencies.

CBM offers advantages over step-and-shoot scans, e.g. more uniform axial sensitivities, and more freedom in scanning ranges, as scans are no longer bound to discrete numbers of bed positions (*19*). CBM also supports different speed profiles, e.g. allowing slower scans of regions of higher interest, and does not seem to affect motion correction outcomes compared to step-and-shoot (*20*). Finally, patients seem to prefer CBM over step-and-shoot scans (*21*). Thus, offering both DDG and CBM seems desirable, potentially combining the advantages of both. However,

due to the additional time dependencies, conventional DDG algorithms cannot be expected to work properly per se, and need – at least – modifications for CBM. For example, center-of-mass-based algorithms work well with moving tracer accumulations within the scanner (e.g., the heart in ^{18}F-FDG PET scans ([11])), but would fail when these enter or leave the field-of-view during CBM.

In this study we investigated how a dedicated CBM-DDG algorithm performs in comparison to a conventional belt system. Originally, first implementations were developed for step-and-shoot acquisitions ([10]), but it was then extended to dynamic PET characterized by non-stationary tracer distributions ([22]). Prior investigation demonstrated its CBM compatibility ([23]). Additionally, it potentially avoids the problem of gating signal inversion inherent to DDG in step-and-shoot scans of adjacent bed positions ([24,25]). Therefore, this study assessed its performance in a cohort of routine patients undergoing whole-body ^{18}F-FDG CBM-PET/CT.

MATERIALS AND METHODS

Patient Data

Datasets of 56 patients with suspected malignancies in thorax or abdomen who underwent ^{18}F-FDG CBM-PET/CT scans between December 2018 and July 2019 were included in this analysis. All patients gave written informed consent for retrospective examination. This study was approved by the ethics committee of the Ärztekammer Westfalen-Lippe and the University of Münster (AZ 2019-024-f-S), and performed in accordance with the 1964 Helsinki declaration and its later amendments.

PET/CT Scan

The patients fasted overnight before PET/CT. ^{18}F-FDG (4 MBq/kg body mass i.v.) was injected ≈1 h prior to scanning. Patients were then scanned on a Biograph mCT (Siemens Healthcare GmbH, Erlangen, Germany) capable of time-of-flight and CBM (axial PET field-of-view, 21.8 cm; spatial resolution at center, 4 mm full-width at half-maximum; sinogram sizes, 400x168; time-of-flight bins, 13) (26). Scanning was performed in supine position with the arms above the head. During examination, the respiratory gating system AZ-733 V (Anzai Co., Tokyo, Japan) recorded respiratory signals subsequently used for gating (belt gating, BG).

Patients were scanned from head or neck down to the proximal femur. Based on topograms, low-dose CT scans in end-expiration were performed (tube voltage, 120 kV; effective current, 18 mAs; slice thickness, 3.0 mm; duration, 10–20 s), followed by list mode PET in CBM (free breathing; speed, 1.1 mm/s; duration, 560–1270 s).

Gating and Reconstructions

The DDG algorithm investigated is based on a spectral analysis of PET data (*23*). These were first projected into a series of 500 ms 3D volumes by histogramming each prompt event into the voxel corresponding to the center of the time-of-flight bin, on a grid with 32x32 transaxial voxels, and axially-extended to full acquisition length using 2 mm slices. Delayed events do not contain localized motion information and were ignored. The acquisition was then divided into overlapping axial regions of 80 mm length, and the spectral analysis method was used to determine a mask identifying which voxels were subject to respiratory motion. To this end, we defined an initial estimate of respiratory amplitude, $r_{AP}(t)$, as the change in anterior-posterior distribution of counts over time. The anterior-posterior distribution at time t is defined as the standard deviation SD of the corresponding 500 ms 3D volume, $g_{xyz}(t)$, projected onto the anterior-posterior axis:

$$r_{AP}(t) = SD\left[\sum_x \sum_z g_{xyz}(t)\right]. \qquad (1)$$

The respiratory frequency was then defined as

$$f_{resp} = \text{argmax}\{R_{AP}(f)\} \qquad (2)$$

for all frequencies in the range 0.125 Hz $< f <$ 0.5 Hz, where $R_{AP}(f)$ is the power spectrum of r_{AP}. Cardiac frequencies were thus excluded. The location xyz for 80 mm range n was included in the mask $\omega_{xyz,n}$ (i.e., $\omega_{xyz,n} \neq 0$) for the corresponding range if

$$\text{argmax}\{G_{xyz,n}(f)\} > thresh \qquad (3)$$

for frequencies in the range $f_{resp} - 0.05$ Hz $< f_{resp} < f_{resp} + 0.05$ Hz, where $G_{xyz,n}(f)$ is the power spectrum of the 3D volume at range n, $g_{xyz,n}(t)$, in the temporal domain, and $thresh$ was determined iteratively such that 10% of pixels were included in the mask.

A weighting function was required to identify the relative direction that regions of contrast (edges) move (*10*). By assigning positive or negative weights to mask values from edges that are respectively opposed in the direction of motion, the net contribution from moving edges add constructively to the overall respiratory signal. The weighted mask value at each voxel of region n within the mask was defined as

$$\omega_{xyz,n} = \cos(\phi_{xyz,n} - \Phi_{\max,n}), \qquad (4)$$

where $\phi_{xyz,n}$ is the phase angle at f_{resp}, the peak frequency of respiration derived from the spectral analysis, and $\Phi_{\max,n}$ is the mode phase angle of all corresponding voxels in the mask.

The relationship between signal gradient sign and the absolute direction of motion is arbitrary and independent for different axial bed positions (*24,25*), so for CBM acquisitions, phase angles for region n were offset by the optimal angle $\Phi_{opt,n}$ which minimized the difference between weights in adjacent, overlapping regions:

$$\Phi_{opt,n} = \text{argmin}\{\Sigma_{x,y,z}(\phi_{xyz,n} - \phi_{xyz,m})^2\}. \qquad (5)$$

To initialize equation (5), $\Phi_{opt,n}$ was set to 0 for region $n = 0$, defined as the axially central 80 mm region, and m refers to the adjacent region in the direction of the axial center,

$$m = \text{sgn}(n)(|n| - 1). \qquad (6)$$

The phase-weighted masks $\omega_{xyz,n}$ from all 80 mm regions were combined into a single mask representing the entire axial extent, $\omega_{xyz,avg}$, by averaging the non-zero values at xyz, i.e.,

$$\omega_{xyz,avg} = \frac{1}{\text{Number of } n \text{ with } \omega_{xyz,n} \neq 0} \Sigma_n \, \omega_{xyz,n}. \qquad (7)$$

The respiratory signal $x_{DDG0}(t)$ was obtained by summing all values in the masked time series of 3D volumes, $g_{xyz}(t)$, such that

$$x_{DDG0}(t) = \sum_{x,y,z} \omega_{xyz,avg} \cdot g_{xyz}(t). \qquad (8)$$

Changes in anterior-posterior motion in the volume series were used to ensure the signal increases/decreases during inspiration/expiration, respectively. Low frequency changes in signal offset and amplitude that result from large axial variations in tracer distribution were removed by subtracting a fitted spline,

$$x_{DDG1}(t) = x_{DDG0}(t) - \text{spline}(t), \qquad (9)$$

and normalized using a $w = 15$ s sliding window,

$$x_{DDG}(t) = \frac{x_{DDG1}(t)}{SD[x_{DDG1}(t-w:t+w)]}, \qquad (10)$$

where SD is the standard deviation of the window.

Finally, the signals were linearly interpolated to 50 Hz. BG signals $x_{BG}(t)$ were recorded at 50 Hz.

Both $x_{BG}(t)$ and $x_{DDG}(t)$ were corrected for baseline drifts to eliminate non-respiratory motion. This was done by subtracting a smoothed step function defined on intervals of 15 s length representing the 5th percentile of the original signal. This also ensured similar amounts of noise for different axial positions in amplitude-gated CBM images (although potentially resulting in residual blur by non-compensated baseline motion). The "optimal gates" (OG) with 35% of the measured PET data corresponding to the smallest signal amplitude interval were reconstructed (*27*).

Additionally, images were reconstructed using an elastic motion correction algorithm (EMOCO) (*28*). First, motion vectors between OG and static reconstructions were determined using optical flow estimation. These vectors were then treated as blurring kernels in the forward

projection of the reconstruction, effectively de-blurring motion effects (*29*). This algorithm has been validated against an established gate-to-gate motion correction (*30*).

All datasets were reconstructed using the e7 toolbox (Siemens Healthcare GmbH, Erlangen, Germany) by ordinary Poisson ordered subset expectation maximization (3 iterations, 21 subsets) with point-spread-function, time-of-flight, normalization, random and scatter corrections, resulting in the following reconstructions: static; optimally-gated (BG-OG, DDG-OG, respectively); and fully motion-corrected (BG-EMOCO, DDG-EMOCO, respectively). Attenuation correction was based on CT data. The images comprised slices of 400x400 voxels (volume, 2.04x2.04x2.03 mm^3). No post-reconstruction filter was applied.

Data Analysis

$x_{BG}(t)$ and $x_{DDG}(t)$ were analyzed by calculating the global Pearson correlation coefficient r_{global} taking all time indices t into account.

Furthermore, regional correlation coefficients r_{regional} were determined for these ranges: R0 – below bladder; R1 – bladder to right kidney; R2 – right kidney to liver dome; R3 – liver dome to aortic arch; R4 – aortic arch to lung apex; R5 – above lung apex (Table 1). The positions of these landmarks were determined from CT, and the times when they were in the center of the PET scanner were calculated.

Finally, local correlation coefficients $r_{\text{local}}(t_0)$ were calculated for every time t_0 as the correlation coefficient between $x_{BG}(t)$ and $x_{DDG}(t)$ determined for $t_0 - 5\,s < t < t_0 + 5\,s$, i.e., on a 10 s interval around t_0, resulting in a better resolved correlation metric than r_{regional}.

The reconstructed PET images were analyzed for lesions between bladder and lung apex. These were characterized individually for all reconstructions by their maximum standardized

uptake value SUV_{max}, their apparent metabolic volume $V_{50\%}$ based on the respective 50% SUV_{max} threshold, and their mean standardized uptake SUV_{mean} in that volume. SUV_{max} was determined in a region-of-interest manually placed over the respective lesion. Since multiple lesions were potentially derived from a scan, one lesion per acquisition was randomly chosen, defining a subgroup that was additionally analyzed.

Finally, identically color-scaled coronal slices through the lesions of this subgroup were prepared for an assessment of visual differences between static reconstructions, BG-EMOCO, and DDG-EMOCO, and between BG-OG and DDG-OG. These slices were presented independently in random order to two nuclear medicine clinicians and one medical physicist who were asked to rate the relative quality in terms of lesion delineation without knowledge of the actual reconstruction method. A relative score was devised as follows: If a method was judged superior to another, +1 was noted, if it was judged inferior, -1 was noted; else 0 was given. The score values of the experts were averaged for every comparison, and rounded to the nearest integer, resulting in an averaged score per case and comparison.

Statistical Analysis

Correlation coefficients are given as mean values ± standard deviation, SUV_{max}, SUV_{mean} and $V_{50\%}$ as median values ± standard deviation. SUV and volume differences were tested using two-tailed Wilcoxon signed rank tests, while two-tailed sign tests were used to assess visual differences (calculated in MATLAB version 2013b; MathWorks, Natick, MA, USA). Bonferroni corrections for pairwise comparisons were applied; the family-wise error rate was 0.05.

RESULTS

DDG signal calculation typically required 5-10 minutes on a 2.4 GHz, 16 cores, 46 GB RAM system. All 56 signals $x_{DDG}(t)$ demonstrated typical respiratory features between bladder and lung apex; other regions exhibited higher noise levels (Fig. 1A). This was corroborated in the correlation analysis between $x_{BG}(t)$ and $x_{DDG}(t)$ (Fig. 1B). Generally, despite considerable individual variation, r_{local} demonstrated values close to 0 below the bladder, increasing to 0.9 around kidneys and liver, and decreasing to 0 above the lung apex (Fig. 2A).

Regional correlation coefficients r_{regional} consistently showed the highest values in region R2 (0.89±0.07), decreasing to smaller values in R0 and R5 (0.12±0.17 and 0.05±0.08, respectively); r_{global} amounted to 0.48±0.11 (Fig. 2B; Table 1).

In total, 196 lesions were analyzed in 45 of the 56 scans (Table 2). 26 lesions were located in the upper lungs, 13 in the upper mediastinum, 82 in the lower lungs, 20 in the lower mediastinum, 31 in the liver, and 24 in other infradiaphragmatic regions. All lesions were discernible in all reconstructions.

SUV$_{\text{max}}$ for all lesions was 14.3±13.4, 19.8±15.7, and 20.5±15.6 for static reconstructions, BG-EMOCO, and DDG-EMOCO, respectively (Figs. 3 and 4; Table 3). The respective values for SUV$_{\text{mean}}$ were 9.3±9.1, 13.5±11.6, and 13.7±11.4, while the volumes V$_{50\%}$ were 0.5±2.4 mL, 0.3±1.4 mL, and 0.3±1.3 mL. BG-EMOCO and DDG-EMOCO led to significantly different values than static reconstructions. SUV$_{\text{max}}$ was 19.6±17.1 and 18.9±16.6 for BG-OG and DDG-OG, respectively, while SUV$_{\text{mean}}$ was 12.6±12.5 and 12.4±12.2 for BG-OG and DDG-OG, respectively. Volumes were 0.3±1.2 mL (BG-OG) and 0.3±1.3 mL (DDG-OG). No significant differences between BG and DDG were observed.

SUV$_{max}$ in the subgroup of one lesion per scans (n=45) was 9.5±10.5, 13.4±13.5, and 13.5±13.7, SUV$_{mean}$ 6.8±7.1, 8.9±9.4, and 8.9±9.2, and V$_{50\%}$ 0.6±1.8 mL, 0.4±0.6 mL, and 0.3±0.6 mL for static, BG-EMOCO, and DDG-EMOCO images, respectively (Figs. 3 and 4, big dots; Table 4). Differences between static- and either of the EMOCO-derived parameters were highly significant. SUV$_{max}$ was 15.2±14.6 and 14.6±12.5, SUV$_{mean}$ 9.5±10.2 and 9.0±8.3, and V$_{50\%}$ 0.3±0.8 mL and 0.3±0.7 mL for BG-OG and DDG-OG, respectively. Again, no significant differences between BG and DDG were seen.

Visual inspection of the PET images demonstrated improved lesion delineation for both OG and EMOCO compared to static reconstructions, although OG was noticeably noisier (Fig. 5). Quality analysis revealed that static reconstructions was judged superior to BG-EMOCO in a single case, inferior in 33, and equal in 11 cases. Similarly, static reconstructions were judged superior to DDG-EMOCO in no case, inferior in 31, and equal in 14 cases. Both BG-EMOCO and DDG-EMOCO were considered significantly superior to static images ($P<0.001$; Fig. 6). No significant difference was seen between BG and DDG: 8 BG-EMOCO cases were superior to DDG-EMOCO, 5 cases were inferior, 32 cases revealed no difference ($P=0.58$); DDG-OG was superior to BG-OG in 10 cases, inferior in 6 cases, and equal in 29 cases ($P=0.45$; Fig. 6).

DISCUSSION

First clinical studies already demonstrated that DDG methods are equivalent to hardware-based methods in terms of image quality and lesion quantification (*14,15*); accordingly, vendors have started incorporating DDG algorithms into their PET systems (*17*). However, more studies are needed to assure that DDG works well in a wide range of applications, radiotracers, and scanning modes (*31*).

In this respect, our study closes a gap by evaluating a novel CBM-DDG method in a larger patient cohort undergoing whole-body PET. In general, this algorithm resulted in motion-compensated PET images with comparable quality and accuracy as conventional methods, exploiting the advantages of both CBM and DDG in routine scans. An independent study using a similar algorithm but smaller number of datasets (n=15) already demonstrated comparable results, with average regional correlation coefficients r_{regional} of 0.15, 0.69, 0.82, 0.75, 0.46, and 0.07 for regions R0, R1, R2, R3, R4, and R5, respectively (*32*). However, SUV seemed to be smaller for DDG as compared to BG, contrasting our results without significant differences.

Some results of our study are of particular interest. The comparison between $x_{\text{BG}}(t)$ and $x_{\text{DDG}}(t)$ demonstrated considerable correlation even in deep abdominal regions (R0 and R1) in some scans, indicating the presence of respiratory motion there. Unfortunately, only 4 lesions in R1 were detected in our cohort, so no general conclusion can be drawn from the SUV analysis. However, some patients had elevated ^{18}F-FDG uptake in several colon segments; these were visually better defined in both BG- and DDG-derived images than in static images (Fig. 7). A comparison with observations by Walker et al. confirms that respiratory motion plays a significant role in these regions, as they found respiratory information in raw data of regions up to 40 cm below the liver dome (*17*).

In general, good correlations of $x_{\mathrm{BG}}(t)$ and $x_{\mathrm{DDG}}(t)$ were found between bladder and lung apex, making an imaging workflow which automatically corrects for motion between these boundaries possible. Correlation decreases from lung base to apex can be explained by smaller respiratory shifts measured by the DDG algorithm towards the apex. This raises the question of whether motion resolution in the upper lung is still sufficient to compete with belt-derived gating. Surprisingly, an analysis of the lesions located in R4 (n=39) reveals slightly larger median SUV_{max} and SUV_{mean} and smaller $V_{50\%}$ for DDG than for BG (e.g., SUV_{max}: 17.1±15.9 vs. 17.8±15.4 for BG-EMOCO and DDG-EMOCO, respectively). However, this was not statistically significant (with pre-Bonferroni *P* values of 0.05–0.11 for SUV). Larger cohorts are needed to analyze DDG accuracy in the upper lungs. Nevertheless, this would be in line with some observations of hysteresis effects leading to phase differences in respiration between different body regions (*33*).

Our study has some additional limitations. First, only ^{18}F-FDG PET/CT datasets were included. While ^{18}F-FDG is still the most often used radiotracer in clinical scans, other tracers like ligands of the prostate-specific membrane antigen (PSMA) are becoming increasingly popular for PET imaging. It remains to be seen how DDG performs in these scans.

Furthermore, the observed increases in SUV and decreases in volumes are apparently larger than in similar studies (*15,34*). This highlights that lesion quantification is dependent on many factors, especially reconstruction parameters and spatial resolution. We chose to maximize image resolution in order to detect even small differences in performance between BG and DDG. Thus, we did not apply post-reconstruction filters, and reconstructed on a high-resolution grid, leading to higher SUV increases and volume decreases. These values may not represent typical clinical outcomes; they rather reflect maximal differences in SUV and volumes achieved by gating/motion correction within the settings of this study.

CONCLUSION

The investigated DDG algorithm generated accurate respiratory signals from CBM-PET raw data. Gated and motion-corrected images were comparable to a conventional hardware-based approach in terms of lesion quantification and visual quality. The proposed DDG method seems to be a promising motion correction alternative for routine whole-body CBM-PET scans.

KEY POINTS

QUESTION: Is data-driven respiratory gating as accurate as hardware-based approaches in continuous bed motion PET?

PERTINENT FINDINGS: This study demonstrates no significant difference in lesion quantification and visual quality between data-driven and hardware-based gating, while both methods outperform static reconstructions.

IMPLICATIONS FOR PATIENT CARE: The presented data-driven gating method for continuous bed motion may replace hardware-based approaches, leading to simplifications in workflow and patient management.

REFERENCES

[1] Liu C, Pierce LA, Alessio AM, Kinahan PE. The impact of respiratory motion on tumor quantification and delineation in static PET/CT imaging. *Phys Med Biol*. 2009;54:7345-7362.

[2] Polycarpou I, Tsoumpas C, King AP, Marsden PK. Impact of respiratory motion correction and spatial resolution on lesion detection in PET: a simulation study based on real MR dynamic data. *Phys Med Biol*. 2014;59:697-713.

[3] Guerra L, Ponti E, Morzenti S, et al. Respiratory motion management in PET/CT: applications and clinical usefulness. *Curr Radiopharm*. 2017;10:85-92.

[4] Frood R, McDermott G, Scarsbrook A. Respiratory-gated PET/CT for pulmonary lesion characterisation-promises and problems. *Br J Radiol*. 2018;91:20170640.

[5] Pan T. Respiratory gating in PET/CT: A step in the right direction. *J Nucl Cardiol*. 2018;252:416-418.

[6] Grootjans W, de Geus-Oei LF, Meeuwis AP, et al. Amplitude-based optimal respiratory gating in positron emission tomography in patients with primary lung cancer. *Eur Radiol*. 2014;24:3242-3250.

[7] Lupi A, Zaroccolo M, Salgarello M, et al. The effect of 18F-FDG-PET/CT respiratory gating on detected metabolic activity in lung lesions. *Ann Nucl Med*. 2009;23:191-196.

[8] Kesner AL, Schleyer PJ, Büther F, et al. On transcending the impasse of respiratory motion correction applications in routine clinical imaging – a consideration of a fully automated data driven motion control framework. *EJNMMI Physics*. 2014;1:8.

[9] He J, O'Keefe GJ, Gong SJ, et al. A novel method for respiratory motion gating with geometric sensitivity of the scanner in 3D PET. *IEEE Trans Nucl Sci*. 2008;55:2557-2565.

[10] Schleyer PJ, O'Doherty MJ, Barrington SF, Marsden PK. Retrospective data-driven respiratory gating for PET/CT. *Phys Med Biol*. 2009;54:1935-1950.

[11] Büther F, Dawood M, Stegger L, et al. List mode-driven cardiac and respiratory gating in PET. *J Nucl Med*. 2009;50:674-681.

[12] Kesner AL, Kuntner C. A new fast and fully automated software based algorithm for extracting respiratory signal from raw PET data and its comparison to other methods. *Med Phys*. 2010;37:5550-5559.

[13] Thielemans K, Rathore S, Engbrant F, Razifar P. Device-less gating for PET/CT using PCA. In: 2011 IEEE Nuclear Science Symposium Conference Record, Valencia. IEEE 2011;3904-3910.

[14] Kesner AL, Chung JH, Lind KE, et al. Validation of software gating: a practical technology for respiratory motion correction in PET. *Radiology*. 2016;281:239-248.

[15] Büther F, Vehren T, Schäfers KP, Schäfers M. Impact of data-driven respiratory gating in clinical PET. *Radiology*. 2016;281:229-238.

[16] Walker MD, Bradley KM, McGowan DR. Evaluation of principal component analysis-based data-driven respiratory gating for positron emission tomography. *Br J Radiol*. 2018;91:20170793.

[17] Walker MD, Morgan AJ, Bradley KM, McGowan DR. Evaluation of data-driven respiratory gating waveforms for clinical PET imaging. *EJNMMI Res*. 2019;9:1.

[18] Osborne DR, Acuff S, Cruise S, et al. Quantitative and qualitative comparison of continuous bed motion and traditional step and shoot PET/CT. *Am J Nucl Med Mol Imaging*. 2015;5:56-64.

[19] Panin VY, Smith AM, Hu J, et al. Continuous bed motion on clinical scanner: design, data correction, and reconstruction. *Phys Med Biol*. 2014;59:6153-6174.

[20] Meier JG, Erasmus JJ, Gladish GW, et al. Characterization of continuous bed motion effects on patient breathing and respiratory motion correction in PET/CT imaging. *J Appl Clin Med Phys*. December 9, 2019 [Epub ahead of print].

[21] Schatka I, Weiberg D, Reichelt S, et al. A randomized, double-blind, crossover comparison of novel continuous bed motion versus traditional bed position whole-body PET/CT imaging. *Eur J Nucl Med Mol Imag*. 2016;43:711-717.

[22] Schleyer PJ, Thielemans K, Marsden PK. Extracting a respiratory signal from raw dynamic PET data that contain tracer kinetics. *Phys Med Biol*. 2014;59:4345-4356.

[23] Schleyer PJ, Hong I, Jones J, et al. Data-driven respiratory gating whole body PET using continuous bed motion. In: 2018 IEEE Nuclear Science Symposium and Medical Imaging Conference Proceedings (NSS/MIC), Sydney, Australia. IEEE 2018;1-5.

[24] Schleyer PJ, O'Doherty MJ, Marsden PK. Extension of a data-driven gating technique to 3D, whole body PET studies. *Phys Med Biol*. 2011;56:3953-65.

[25] Bertolli O, Arridge S, Wollenweber SD, et al. Sign determination methods for the respiratory signal in data-driven PET gating. *Phys Med Biol*. 2017;62:3204-3220.

[26] Jakoby BW, Bercier Y, Conti M, et al. Physical and clinical performance of the mCT time-of-flight PET/CT scanner. *Phys Med Biol*. 2011;56:2375-2389.

[27] van Elmpt W, Hamill J, Jones J, et al. Optimal gating compared to 3D and 4D PET reconstruction for characterization of lung tumours. *Eur J Nucl Med Mol Imaging*. 2011;38:843-855.

[28] Hong I, Jones J, Hamill J, et al. Elastic motion correction for continuous bed motion whole-body PET/CT. In: 2016 IEEE Nuclear Science Symposium, Medical Imaging Conference and

Room-Temperature Semiconductor Detector Workshop (NSS/MIC/RTSD), Strasbourg. IEEE 2016;1-2.

[29] Hong I, Jones J, Casey M. Ultrafast elastic motion correction via motion deblurring. In: 2014 IEEE Nuclear Science Symposium and Medical Imaging Conference (NSS/MIC), Seattle, WA. IEEE 2014;1-2.

[30] Pösse S, Hong I, Mannweiler D, et al. Respiratory motion compensation in PET/CT: evaluation of an elastic motion compensation technique based on motion deblurring. *Nuklearmedizin*. 2018;57:A52.

[31] Kesner AL, Ross Schmidtlein C, Kuntner C. Real-time data-driven motion correction in PET. *EJNMMI Physics*. 2019;6:3.

[32] Meier J, Schleyer PJ, Judson J, et al. Evaluation of a novel data driven gating technique for PET/CT imaging with continuous bed motion. *J Nucl Med*. 2019;60(S1):523.

[33] Dasari PKR, Shazeeb MS, Könik A, et al. Adaptation of the modified Bouc–Wen model to compensate for hysteresis in respiratory motion for the list-mode binning of cardiac SPECT and PET acquisitions: Testing using MRI. *Med Phys*. 2014;41:112508.

[34] Werner MK, Parker JA, Kolodny GM, et al. Respiratory gating enhances imaging of pulmonary nodules and measurement of tracer uptake in FDG PET/CT. *AJR Am J Roentgenol*. 2009;193:1640-1645.

TABLES

Table 1: Definition of regions and correlation coefficients (mean ± standard deviation, range) between BG and DDG signals

Region	R0	R1	R2	R3	R4	R5	Global
Start	Proximal femur	Bladder	Right kidney	Liver dome	Aortic arch	Lung apex	Proximal femur
End	Bladder	Right kidney	Liver dome	Aortic arch	Lung apex	Head/neck	Head/neck
Correlation coefficients	0.12±0.17 (-0.12–0.61)	0.72±0.15 (0.35–0.96)	0.89±0.07 (0.68–0.97)	0.77±0.16 (0.26–0.94)	0.41±0.32 (-0.71–0.86)	0.05±0.08 (-0.15–0.21)	0.48±0.11 (0.30–0.75)

Table 2: Lesion characteristics; SUV and volumes (median ± standard deviation, range) determined from static reconstructions

Region	Number of lesions/patients	SUV_{max}	SUV_{mean}	$V_{50\%}$ [mL]
Upper lungs	26/14	12.5±16.1 (5.1–84.1)	8.1±10.3 (3.4–52.1)	0.2±0.7 (0.0–2.6)
Upper mediastinum	13/10	18.3±10.9 (5.7–38.9)	12.4±7.4 (3.4–25.9)	0.8±1.5 (0.1–5.4)
Lower lungs	82/32	12.9±15.8 (3.0–88.0)	8.5±10.9 (2.0–58.8)	0.4±1.7 (0.1–11.5)
Lower mediastinum	20/16	14.1±12.5 (5.5–57.4)	9.2±9.0 (3.6–41.9)	0.4±1.1 (0.1–3.6)
Liver	31/11	14.5±6.0 (7.1–26.9)	9.0±3.8 (4.4–17.6)	1.5±3.8 (0.1–14.4)
Other infradiaphragmatic regions	24/10	20.4±9.3 (7.8–43.0)	13.6±6.1 (4.9–28.0)	0.8±3.0 (0.1–12.0)
Total	196/45	14.3±13.4 (3.0–88.0)	9.3±9.1 (2.0–58.8)	0.5±2.4 (0.0–14.4)

Table 3: Characteristics of all 196 lesions (median ± standard deviation) for all correction strategies

	Static	BG-EMOCO	DDG-EMOCO	BG-OG	DDG-OG
SUV_{max}	14.3±13.4	19.8±15.7	20.5±15.6	19.6±17.1	18.9±16.6
P value to static		<0.001	<0.001		
P value to BG			0.60		0.19
SUV_{mean}	9.3±9.1	13.5±11.6	13.7±11.4	12.6±12.5	12.4±12.2
P value to static		<0.001	<0.001		
P value to BG			0.65		0.11
$V_{50\%}$ [mL]	0.5±2.4	0.3±1.4	0.3±1.3	0.3±1.2	0.3±1.4
P value to static		<0.001	<0.001		
P value to BG			0.87		0.50

BG: belt gating, DDG: data-driven gating, EMOCO: elastic motion correction, OG: optimal gating

Table 4: Characteristics of the 45 randomly chosen lesions (median ± standard deviation) for all correction strategies

	Static	BG-EMOCO	DDG-EMOCO	BG-OG	DDG-OG
SUV$_{max}$	9.5±10.5	13.4±13.5	13.5±13.7	15.2±14.6	14.6±12.5
P value to static		<0.001	<0.001		
P value to BG			0.21		0.28
SUV$_{mean}$	6.8±7.1	8.9±9.4	8.9±9.2	9.5±10.2	9.0±8.3
P value to static		<0.001	<0.001		
P value to BG			0.44		0.20
V$_{50\%}$ [mL]	0.6±1.8	0.4±0.6	0.3±0.6	0.3±0.8	0.3±0.7
P value to static		<0.001	<0.001		
P value to BG			0.71		0.33

BG: belt gating, DDG: data-driven gating, EMOCO: elastic motion correction, OG: optimal gating
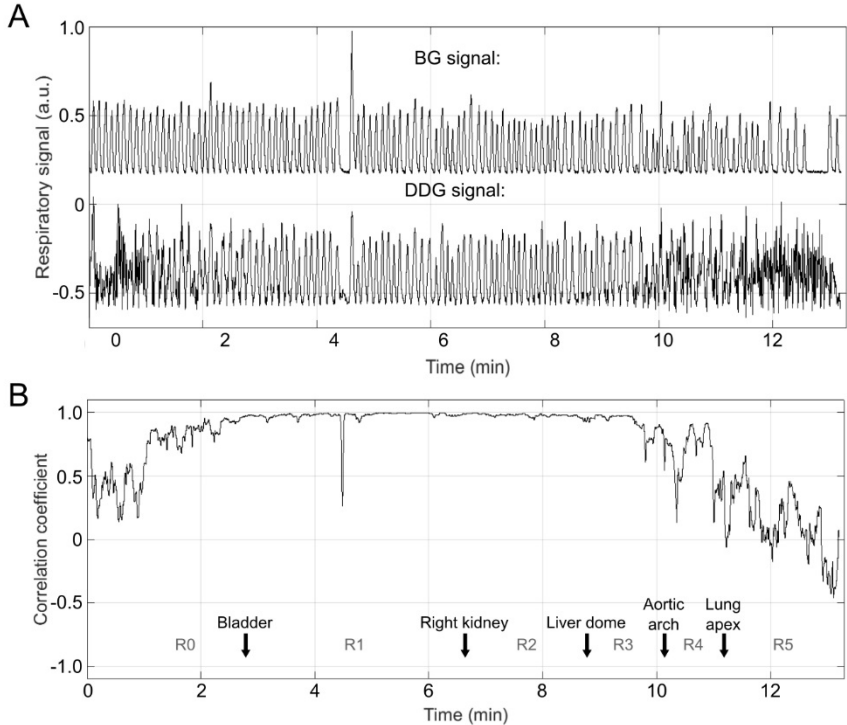
Figure 1: Comparison of respiratory signals (A) and correlation coefficient r_{local} (B) for a typical case (landmarks passing the scanner center indicated by arrows; regions designated by R0, …, R5).
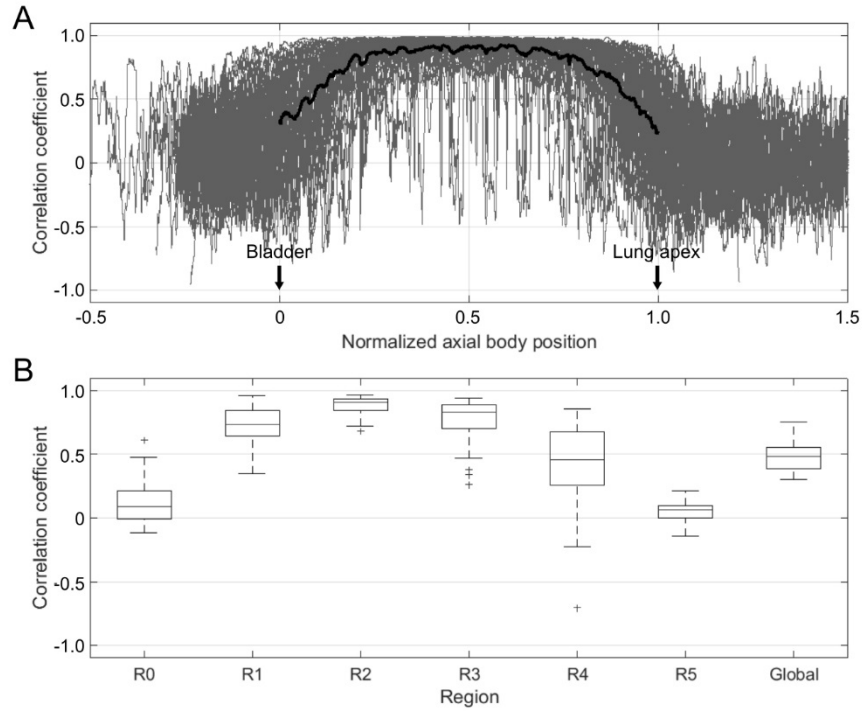
Figure 2: Superposition of correlation coefficients r_{local} (gray) for all scans in normalized axial position (0: bladder, 1: lung apex) (A; average in black); boxplot of correlation coefficients r_{regional} for all scans (B; asterisks denote outliers).
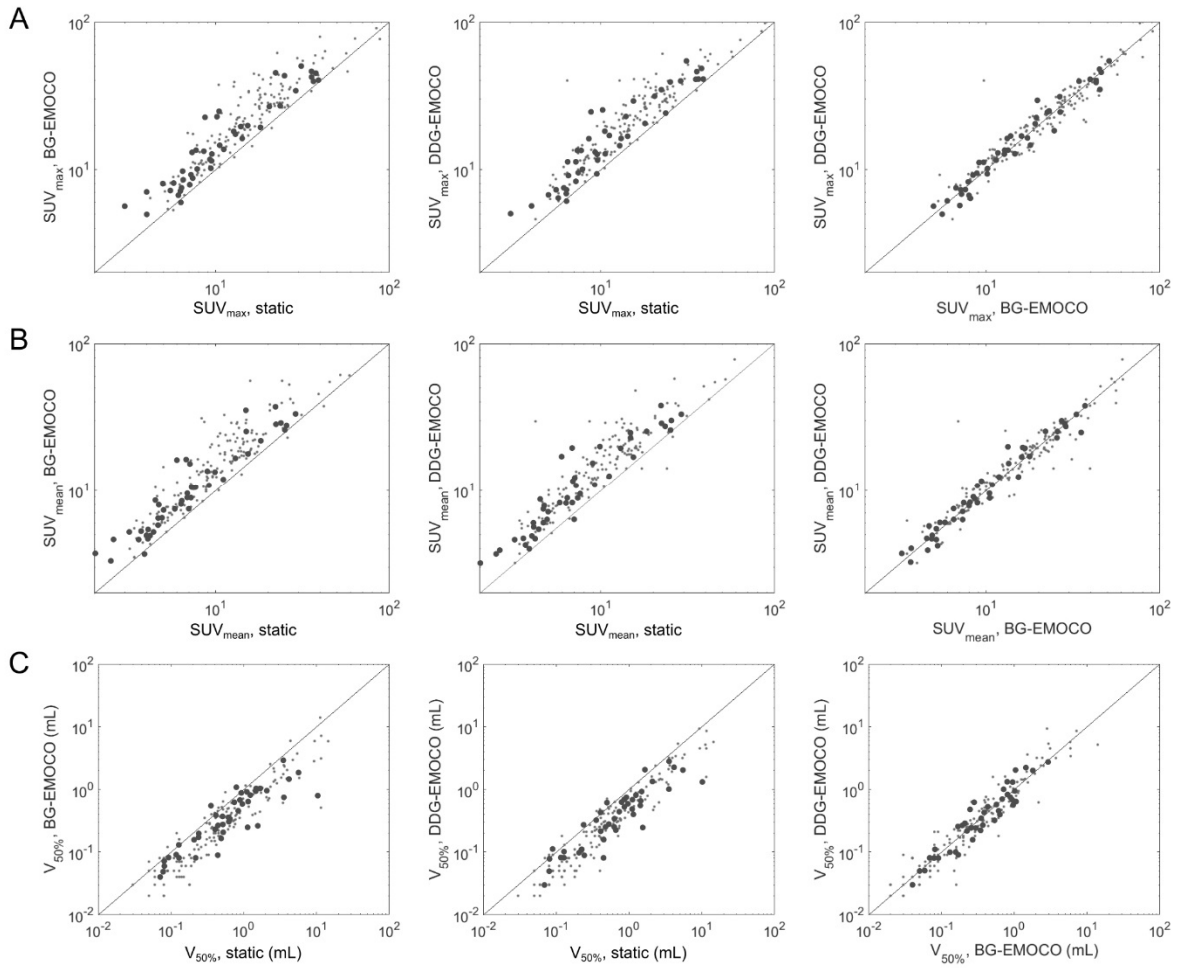
Figure 3: Scatter plots of SUV_{max} (A), SUV_{mean} (B), and $V_{50\%}$ (C) for static, BG-EMOCO, and DDG-EMOCO reconstructions. Subgroup of one lesion per scan denoted by big dots; black line: identity.
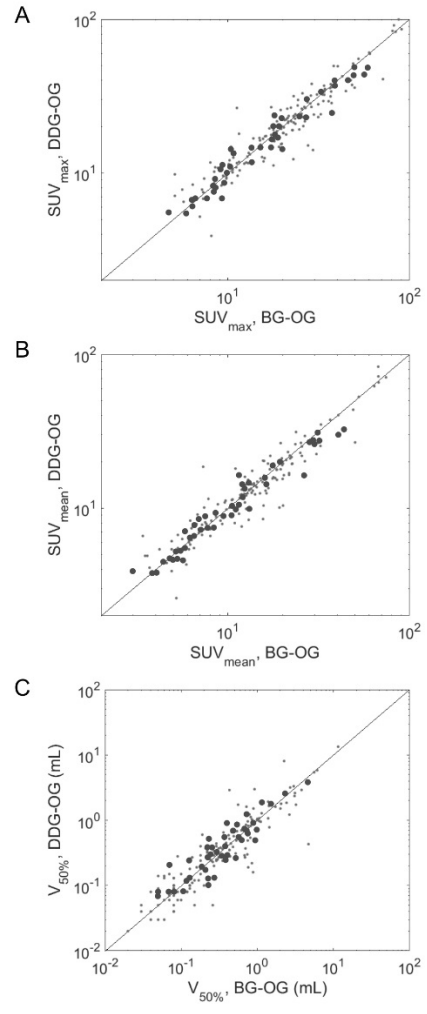
Figure 4: Scatter plots of SUV_{max} (A), SUV_{mean} (B), and $V_{50\%}$ (C) for BG-OG, and DDG-OG reconstructions. Subgroup of one lesion per scan denoted by big dots; black line: identity.
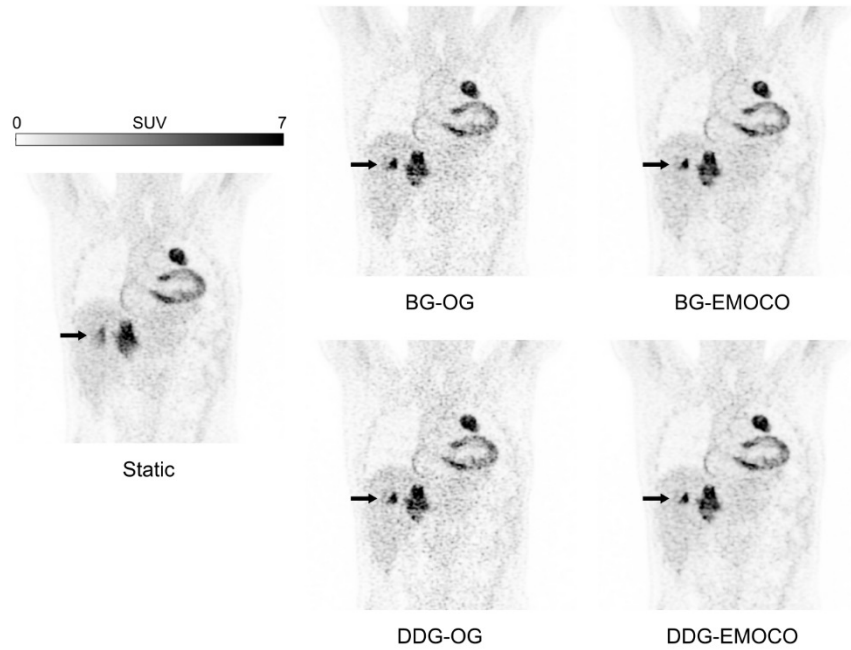
Figure 5: Typical outcome of gating (OG) and motion correction (EMOCO) using BG and DDG signals, compared to the static reconstruction. Visual improvements of liver lesions (arrows) are apparent.
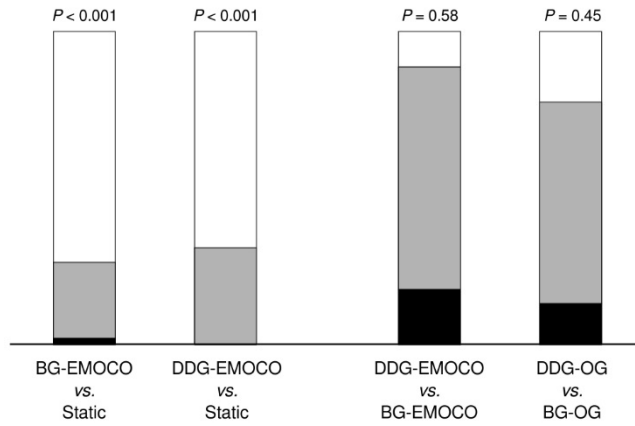
Figure 6: Pairwise visual quality comparison between EMOCO and static reconstructions (left), and DDG and BG (right), respectively (n=45). White areas denote cases where method 1 was superior to method 2, black areas cases where method 1 was inferior; gray areas denote cases of equal quality.
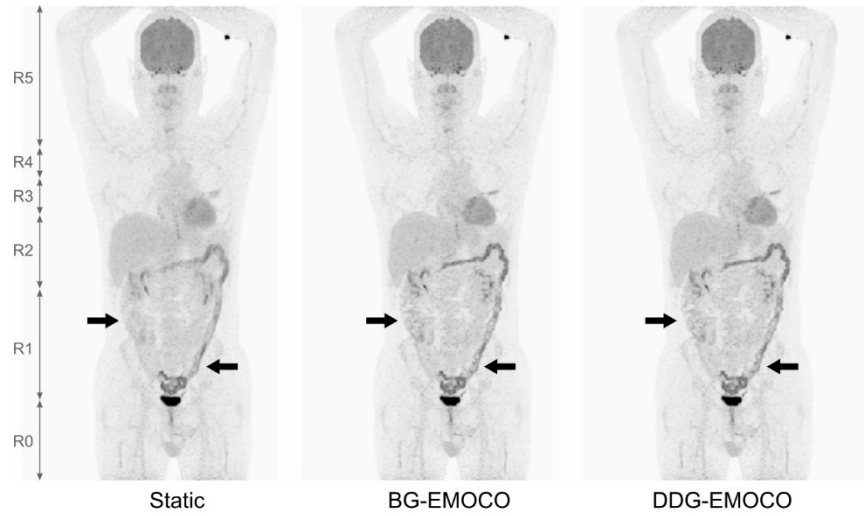
Figure 7: Maximum intensity projection of a scan with elevated colon uptake (arrows; regions R1 and R2) demonstrating better delineation with BG and DDG.